Supplement of Geosci. Model Dev., 15, 4831–4851, 2022
https://doi.org/10.5194/gmd-15-4831-2022-supplement

Geoscientific Model Development
Open Access
EGU

Supplement of

Variational inverse modeling within the Community Inversion Framework v1.1 to assimilate $\delta^{13}C(CH_4)$ and CH_4: a case study with model LMDz-SACS

Joël Thanwerdas et al.

Correspondence to: Joël Thanwerdas (joel.thanwerdas@lsce.ipsl.fr)

Supplementary material can be found here. References regarding the selected isotopic signature values are compiled in Text S1. Methods and references used to prescribe the CH_4 sinks are presented in Text S2. A demonstration of the equation used to infer an isotopic signature for the soil uptake is provided in Text S3. Adjoint tests are provided in Text S4. Details regarding the stations that provided the assimilated data are given in Table S3 and Table S4. Emission and source signature values for each scenario are given in Table S5 and Table S6, respectively. Finally, multiple additional figures mentioned in the main paper are also provided.

1 Text S1 : Source signature references

Data from literature have been compiled to assess region-specific or global values for isotopic source signatures associated to the multiple categories introduced in the main paper. We provide here some additional information on the prescribed source signatures of several sub-categories that were not mentioned in the main text.

Rice cultivation: Bréas et al. (2001) provided a range between -68 ‰ and -48 ‰ $\delta^{13}C(CH_4)_{source}$ for $CH4$ emitted from rice paddies. For this work, we chose a value of -63 ‰ (Rice et al., 2016; Bousquet et al., 2006).

Waste: Waste sector encompasses three different source categories : waste water ($\sim$ 49 % of the total emissions from this category), solid waste ($\sim$ 49 %), agriculture waste burning and ($\sim$ 2 %). Values of -48 ‰ for waste water, -52 ‰ for solid waste and -23.6 ‰ for agriculture waste burning (Levin et al., 1993; Yamada et al., 2006; Townsend-Small et al., 2012; Bergamaschi et al., 1998; Chanton et al., 1999) were taken.

Biofuels-biomass burning: Biofuels-biomass burning sector encompasses four very different emission sectors : biomass burning ($\sim$ 35 %), biofuel burning ($\sim$ 40 %), energy use ($\sim$ 20 %) and fossil fuel fires ($\sim$ 5 %). We applied regional values for biomass burning ranging between -26.5 ‰ and -15.46 ‰ (see Table S1), a global value of -20 ‰ for biofuel burning and a global value of -30 ‰ for energy use (Chanton et al., 2000).

Oceanic fluxes: $\delta^{13}C(CH_4)_{source}$ values from various oceans in the world were found in a small range: roughly -44 ‰ to -40 ‰ (Brunskill et al., 2011; Holmes et al., 2000; Sansone et al., 2001). A value of -42 ‰ was used.

Termites: A wide range of $\delta^{13}C(CH_4)_{source}$ signatures have been reported in the literature, from -93.8 ‰ to -54 ‰ (Bréas et al., 2001). For these simulations, a value of -63 ‰was taken.

Geological fluxes (onshore): We used a value of -50 ‰ (Bousquet et al., 2006).

2 Text S2 : CH_4 sinks and associated KIEs in LMDz-SACS

CH_4 is removed in LMDz-SACS through the following chemical reactions with OH, O(^{1}D) and Cl:

$$\mathrm{CH_4 + OH} \rightarrow \mathrm{CH_3 + H_2O} \quad \text{(R1)}$$

$$\mathrm{CH_4 + Cl} \rightarrow \mathrm{CH_3 + HCl} \quad \text{(R2)}$$

$$\mathrm{CH_4 + O(^1D)} \rightarrow \mathrm{CH_3 + OH} \quad \text{(R3)}$$

$$\mathrm{CH_4 + O(^1D)} \rightarrow \mathrm{H_2 + CH_2O} \quad \text{(R4)}$$

We use the new chemistry parsing system introduced in the main paper to represent the chemical reactions with OH, O(^{1}D) and Cl. Fractionation values (KIE for Kinetic Isotope Effect) are prescribed to the different sinks. Here, KIE $= k_{12}/k_{13}$ where k_{12} is the constant rate of the reaction involving $^{12}CH_4$ and k_{13} is the constant rate of the same reaction involving $^{13}CH_4$.

The three-dimensional and time-dependent oxidant concentration fields (OH, O(^{1}D) and Cl) were simulated by the LMDz General Circulation Model (GCM) coupled to the chemistry and aerosol model INCA (INteraction with Chemistry and Aerosols, Folberth et al., 2006; Hauglustaine et al., 2004). The mean tropospheric Cl have been scaled to that inferred by Wang et al. (2019), i.e. 620 $\mathrm{atoms\,cm^{-3}}$.

Reaction constants in this paper are taken from Burkholder et al. (2015) and KIEs from Saueressig et al. (1995) for the reaction with Cl and from Saueressig et al. (2001) for reactions with OH and O(^{1}D). All reaction constants and associated values are reported in Table S2. Few studies have focused on assessing KIEs associated with CH_4 chemical sinks (especially for O(^{1}D) and Cl) within a wide temperature range and thus significant uncertainties still remain. We chose the KIE values for CH_4 + OH from Saueressig et al. (2001) as they indicate that this data is of considerably higher precision and experimental reproductibility than earlier studies, in particular Cantrell et al. (1990).

The CH_4 atmospheric lifetime relative to chemical destruction is the ratio of the total CH_4 atmospheric burden to the atmospheric sink due to the chemical reactions with OH, O(^{1}D) and Cl. Our fields lead to an atmospheric chemical lifetime of 9.16 ± 0.12 years.

The soil uptake is accounted for as a negative source using the estimates taken from Ridgwell et al. (1999). Therefore we define an effective $\delta^{13}\mathrm{C(CH_4)_{source,eff}}$ signature ($\delta^{13}\mathrm{C(CH_4)}$) based on the KIE of the soil uptake ($\mathrm{KIE_{soil}}$) and the observed $\delta^{13}\mathrm{C(CH_4)_{atm}}$ at the surface :

$$\delta^{13}\mathrm{C(CH_4)_{source,eff}} = \frac{1 + \delta^{13}\mathrm{C(CH_4)_{atm}}}{\mathrm{KIE_{soil}}} - 1 \quad (1)$$

$\delta^{13}\mathrm{C(CH_4)_{source,atm}}$ denotes the atmospheric isotopic signal near the surface. A demonstration is given in Text S3. A $\mathrm{KIE_{soil}}$ of 1.020 is chosen based on multiple studies (Snover and Quay, 2000; Reeburgh et al., 1997; Tyler et al., 1994; King et al., 1989).

3 Text S3 : Demonstration of effective source signature for the soil uptake

Let L_{12} and L_{13} be the chemical losses of $^{12}CH_4$ and $^{13}CH_4$ through the soil uptake, respectively. k_{12} and k_{13} are the associated reaction constants. M_{12}, M_{13} and M_{air} are the molar masses of $^{12}CH_4$, $^{13}CH_4$ and dry air, respectively. $[^{12}CH_4]$ and $[^{13}CH_4]$ are the atmospheric concentrations of $^{12}CH_4$ and $^{13}CH_4$ at the surface. $\delta^{13}C(CH_4)_{atm}$ is the associated isotopic signal.

KIE_{soil} is defined such that :

$$KIE_{soil} = \frac{k_{12}}{k_{13}} \tag{2}$$

We also have, by definition :

$$L_{12} = k_{12} \cdot [^{12}CH_4] \tag{3}$$

$$L_{13} = k_{13} \cdot [^{13}CH_4] \tag{4}$$

$$[^{13}CH_4] = (1 + \delta^{13}C(CH_4)_{atm}) \cdot R_{std} \cdot [^{12}CH_4] \tag{5}$$

We define $\delta^{13}C(CH_4)_{source,eff}$ the soil uptake effective isotopic signature :

$$\delta^{13}C(CH_4)_{source,eff} = \frac{\frac{L_{13}}{L_{12}}}{R_{std}} - 1 \tag{6}$$

By dividing (3) and (2) and using (4), we can get :

$$\frac{L_{13}}{L_{12}} = \frac{[^{13}CH_4]}{[^{12}CH_4]} \cdot \frac{1}{KIE_{soil}} \tag{7}$$

$$\Rightarrow \delta^{13}C(CH_4)_{source,eff} = \frac{[^{13}CH_4]}{[^{12}CH_4]} \cdot \frac{1}{R_{std}} \cdot \frac{1}{KIE_{soil}} - 1 \tag{8}$$

$$\Rightarrow \delta^{13}C(CH_4)_{source,eff} = \frac{1 + \delta^{13}C(CH_4)_{atm}}{KIE_{soil}} - 1 \tag{9}$$

Defining $\alpha = \frac{1}{KIE_{soil}}$ and assuming that $\epsilon = \alpha - 1 \ll 1$, we find the formula of Snover and Quay (2000) :

$$\delta^{13}C(CH_4)_{source,eff} = \alpha \cdot \delta^{13}C(CH_4)_{atm} + (\alpha - 1) \tag{10}$$

$$\Rightarrow \delta^{13}C(CH_4)_{source,eff} \approx \delta^{13}C(CH_4)_{atm} + \epsilon \tag{11}$$

4 Text S4 : Testing the adjoint code

The adjoint code test is based on the definition of the adjoint observation operator $\boldsymbol{H^*}$:

$$\langle \boldsymbol{H\delta U}, \boldsymbol{H\delta U} \rangle = \langle \boldsymbol{\delta U}, \boldsymbol{H^* H\delta U} \rangle \tag{12}$$

In practice, the vector $\boldsymbol{\delta U} = \lambda \cdot \boldsymbol{U}$ is first provided as an input to the tangent-linear model, with λ being a scalar. After this, the output vector $\boldsymbol{\delta U}$ is retrieved and the first scalar product (left-hand member) is calculated. The adjoint code is then run with this vector as input. The output vector $\boldsymbol{H^* H\delta U}$ of this adjoint code is recovered and the second scalar product is computed. The ratio of these two scalar products is then compared to the machine error (or machine epsilon), here denoted by ϵ, which gives the upper limit of the approximation error caused by the rounding of the calculations of the machine used. The adjoint test value, here denoted by r, is therefore defined by :

$$r = \frac{\frac{\langle \boldsymbol{H\delta U}, \boldsymbol{H\delta U} \rangle}{\langle \boldsymbol{\delta U}, \boldsymbol{H^* H\delta U} \rangle} - 1}{\epsilon} \tag{13}$$

With the LMDz-SACS model, a valid adjoint code should not result in a r exceeding 1000 and this ratio is usually between 1 and 300 for a valid code.

Adjoint tests were performed with a machine error of $2.220446049250313 \times 10^{-16}$ (double-precision). We run two tests involving a two-month simulation based on the REF configuration. Both tests apply an increment λ of 0.2. The first test applied the increment in the control space ($\mathbf{x}$) whereas the second does it in the minimization space ($\chi = \mathbf{B}^{-\frac{1}{2}} \cdot (\mathbf{x} - \mathbf{x}^{\mathrm{b}})$) as explained in Berchet et al. (2021).

The other configurations only modify the input data (fluxes, source signatures, prescribed errors) and do not influence the adjoint operations performed during the inversion, hence we present only the results with REF.

The first test gave a ratio of 50 whereas the second test provided a ratio of 5, proving that the adjoint operations were properly implemented.

Table S1. Regional $\delta^{13}C(CH_4)_{source}$ isotopic signature values for biomass burning taken from (Bousquet et al., 2006).

Region	Biomass burning
Global default	-26.5 ‰
Boreal North America	-26.5 ‰
Temperate North America	-26.5 ‰
Tropical South America	-18.15 ‰
Temperate South America	-19.53 ‰
Africa	-15.46 ‰
Europe	-26.5 ‰
Boreal Asia	-26.82 ‰
Temperate Asia	-19.16 ‰
Southeast Asia	-20.65 ‰
Australia	-26.5 ‰

Table S2. Reaction constants and KIEs of CH_4 chemical sinks. The reaction constants are taken from Burkholder et al. (2015).

Oxidant	KIE	Reference	Reaction constant ($\mathrm{molecule}^{-1}\,\mathrm{s}^{-1}$)
OH	1.0039	Saueressig et al. (2001)	$2.45 \cdot 10^{-12} \cdot \exp(-1775/T)$
Cl	$1.043 \cdot \exp(6.455/T)$	Saueressig et al. (1995)	$7.1 \cdot 10^{-12} \cdot \exp(-1280/T)$
$O(^1D)$ - R3	1.013	Saueressig et al. (2001)	$1.125 \cdot 10^{-10}$
$O(^1D)$ - R4	1.013	Saueressig et al. (2001)	$3.75 \cdot 10^{-11}$

Table S3. List of CH_4 surface in-situ observation sites used in inversions. Marine Boundary Layer (MBL) stations are indicated in red. These stations are used to perform global averages in the main paper.

Site code	Station name	Country/Territory	Network	Latitude	Longitude	Elevation (m a.s.l.)	Date range (MM/YYYY)	**R** error (ppb)
ALT	Alert	Canada	CSIRO EC NOAA	82.45° N	62.50° W	210	01/2012 - 12/2017	8.4
AMS	Amsterdam Island	France	LSCE	37.81° S	77.54° E	8	01/2012 - 12/2017	15.3
AMY	Anmyeon-do	Republic of Korea	KMA	36.54° N	126.33° E	47	01/2012 - 03/2017	9.4
ARH	Arrival Heights	New Zealand	NIWA	77.80° S	166.67° E	184	01/2012 - 02/2016	9.5
ASC	Ascension Island	United Kingdom	NOAA	7.97° S	14.40° W	90	01/2012 - 12/2017	5.9
ASK	Assekrem	Algeria	NOAA	23.26° N	5.63° E	2715	01/2012 - 12/2017	8.3
AZR	Terceira Island	Portugal	NOAA	38.76° N	27.25° W	24	05/2012 - 12/2017	12.7
BHD	Baring Head Station	New Zealand	NIWA NOAA	41.41° S	174.87° E	85	01/2012 - 12/2017	3.7
BKT	Bukit Kototabang	Indonesia	BMG-EMPA NOAA	0.20° S	100.32° E	864	01/2012 - 12/2017	13.2
BMW	Tudor Hill	United Kingdom	NOAA	32.26° N	64.88° W	60	03/2012 - 12/2017	16.1
BRW	Barrow Atmospheric Baseline Observatory	United States	NOAA	71.32° N	156.61° W	3397	01/2012 - 12/2017	14.6
CBA	Cold Bay	United States	NOAA	55.20° N	162.72° W	25	01/2012 - 12/2017	10.7
CFA	Cape Ferguson	Australia	CSIRO	19.28° S	147.06° E	2	01/2012 - 12/2017	3.7
CGO	Cape Grim	Australia	AGAGE CSIRO NOAA	40.68° S	144.69° E	164	01/2012 - 12/2017	8.4
CHR	Christmas Island	Republic of Kiribati	NOAA	1.70° N	157.15° W	5	01/2012 - 12/2017	8.0
CIB	Centro de Investigacion de la Baja Atmosfera (CIBA)	Spain	NOAA	41.81° N	4.93° W	850	01/2012 - 12/2017	14.7
CPT	Cape Point	South Africa	NOAA SAWS	34.35° S	18.49° E	230	01/2012 - 12/2017	10.0
CRZ	Crozet Island	France	NOAA	46.43° S	51.85° E	202	01/2012 - 09/2017	3.6
CYA	Casey	Australia	CSIRO	66.28° S	110.52° E	60	01/2012 - 12/2017	3.0
EIC	Easter Island	Chile	NOAA	27.15° S	109.44° W	42	01/2012 - 04/2017	5.1
ESP	Estevan Point	Canada	EC	49.38° N	126.54° W	120	01/2012 - 12/2016	10.9
GMI	Mariana Islands	Guam	NOAA	13.39° N	144.66° E	6	01/2012 - 06/2017	12.4
HBA	Halley Station	United Kingdom	NOAA	75.60° S	26.33° W	35	01/2012 - 01/2017	4.0
ICE	Storhofdi	Iceland	NOAA	63.40° N	20.29° W	127	01/2012 - 12/2017	8.6
IZO	Izana	Spain	AEMET NOAA	28.31° N	16.50° W	2367	01/2012 - 12/2017	15.1
JFJ	Jungfraujoch	Switzerland	EMPA	46.55° N	7.99° E	1774	01/2012 - 12/2016	10.1

Table S3. List of surface in-situ observation sites used in inversions. *POC stations have been aggregated into a single line but all observations are used in the inversions.

Site code	Station name	Country/Territory	Network	Latitude	Longitude	Elevation (m a.s.l.)	Date range (MM/YYYY)	**R** error (ppb)
KEY	Key Biscayne	United States	NOAA	25.67° N	80.18° W	6	01/2012 - 12/2017	18.0
KUM	Cape Kumukahi	United States	NOAA	19.53° N	154.83° W	8	01/2012 - 12/2017	12.5
LTO	Lamto	Ivory Coast	LSCE	6.22° N	5.03° W	155	01/2012 - 12/2017	15.5
MAA	Mawson Station	Australia	CSIRO	67.62° S	62.87° E	32	01/2012 - 12/2016	3.6
MEX	High Altitude Global Climate Observation Center	Mexico	NOAA	18.98° N	97.31° W	4469	01/2012 - 12/2017	13.9
MHD	Mace Head	Ireland	AGAGE LSCE NOAA	53.33° N	9.90° W	155	01/2012 - 12/2017	15.8
MID	Sand Island	United States	NOAA	28.21° N	177.37° W	8	01/2012 - 12/2017	14.2
MLO	Mauna Loa	United States	CSIRO NOAA	19.54° N	155.58° W	3397	01/2012 - 12/2017	13.6
MQA	Macquarie Island	Australia	CSIRO	54.48° S	158.97° E	12	01/2012 - 12/2016	3.3
MWO	Mt. Wilson Observatory	United States	NOAA	34.22° N	118.06° W	1774	01/2012 - 12/2017	15.0
NAT	Farol De Mae Luiza Lighthouse	Brazil	NOAA	5.64° S	35.23° W	20	01/2012 - 12/2017	10.0
NMB	Gobabeb	Namibia	NOAA	23.58° S	15.03° E	461	01/2012 - 12/2017	10.1
NWR	Niwot Ridge	United States	NOAA	40.05° N	105.59° W	3526	01/2012 - 12/2017	16.3
PAL	Pallas-Sammaltunturi	Finland	FMI NOAA	67.97° N	24.12° E	230	01/2012 - 12/2017	10.5
POC*	Pacific Ocean	N/A	NOAA	35° S - 30° N	178°W - 178° E	20	01/2012 - 07/2017	10.2
PON	Pondichery	India	LSCE	12.01° N	79.86° E	30	01/2012 - 03/2015	10.0
PSA	Palmer Station	United States	NOAA	64.77° S	64.05° W	15	01/2012 - 12/2017	3.3
RPB	Ragged Point	Barbados	AGAGE NOAA	13.17° N	59.43° W	45	01/2012 - 12/2017	11.3
SEY	Mahe Island	Seychelles	NOAA	4.68° S	55.53° E	7	01/2012 - 12/2017	11.8
SHM	Shemya Island	United States	NOAA	52.72° N	174.11° E	28	01/2012 - 11/2017	8.6
SMO	Tutuila	American Samoa	AGAGE NOAA	14.25° S	170.57° W	1774	01/2012 - 12/2017	7.3
SPO	South Pole	United States	CSIRO NOAA	89.98° S	24.80° W	2810	01/2012 - 12/2017	3.1
STR	Sutro Tower	United States	NOAA	37.76° N	122.45° W	486	01/2012 - 12/2017	10.0
SUM	Summit	Greenland	NOAA	72.60° N	38.42° W	3214	01/2012 - 07/2017	7.5
SYO	Syowa Station	Japan	NOAA	69.00° S	39.58° E	16	01/2012 - 01/2017	3.1
TDF	Tierra Del Fuego	Argentina	NOAA	54.87° S	68.48° W	20	01/2012 - 12/2013	3.6

Table S3. List of surface in-situ observation sites used in inversions. *WPC stations have been aggregated into a single line but all observations are used in the inversions.

Site code	Station name	Country/Territory	Network	Latitude	Longitude	Elevation (m a.s.l.)	Date range (MM/YYYY)	$\mathbf{R}$ error (ppb)
TER	Teriberka	Russian Federation	MGO	69.20° N	35.10° E	40	01/2012 - 12/2016	10.0
THD	Trinidad Head	United States	AGAGE NOAA	41.05° N	124.15° W	120	01/2012 - 06/2017	11.3
TIK	Hydrometeorological Observatory of Tiksi	Russia	MGO NOAA	71.60° N	128.89° E	8	01/2012 - 12/2016	10.0
TR3	Traînou	France	LSCE	47.96° N	2.11° E	8	01/2012 - 12/2017	15.5
USH	Ushuaia	Argentina	NOAA	54.85° S	68.31° W	32	01/2012 - 12/2017	9.9
UTA	Wendover	United States	NOAA	39.90° N	113.72° W	1332	01/2012 - 12/2017	17.3
UUM	Ulaan Uul	Mongolia	NOAA	44.45° N	111.10° E	1012	01/2012 - 12/2017	12.7
WIS	Weizmann Institute of Science at the Arava Institute	Israel	NOAA	30.63° N	34.85° E	482	01/2012 - 12/2017	18.8
WKT	Moody	United States	NOAA	31.32° N	97.33° W	708	01/2012 - 12/2017	15.0
WLG	Mt. Waliguan	Peoples Republic of China	CMANOAA	36.28° N	100.91° E	3815	01/2012 - 12/2017	12.1
WPC*	Western Pacific Cruise	N/A	NOAA	30° S - 30° N	137° E - 170° E	10	06/2012 - 06/2013	9.9
ZEP	Ny-Alesund	Norway and Sweden	NOAA	78.91° N	11.89° E	479	01/2012 - 12/2017	9.3

Table S4. List of $\delta^{13}C(CH_4)$ surface in-situ observation sites used in inversions. MBL stations are indicated in red. These stations are used to perform global averages in the main paper.

Site code	Station name	Country/Territory	Network	Latitude	Longitude	Elevation (m a.s.l.)	Date range (MM/YYYY)	**R** error (‰)
ALT	Alert	Canada	NOAA/INSTAAR	82.45° N	62.50° W	195	01/2012 - 12/2017	0.12
AMY	Anmyeon-do	Republic of Korea	NOAA/INSTAAR	36.54° N	126.33° E	125	12/2013 - 12/2017	0.20
ASC	Ascension Island	United Kingdom	NOAA/INSTAAR	7.97° S	14.40° W	90	01/2012 - 12/2017	0.12
AZR	Terceira Island	Portugal	NOAA/INSTAAR	38.76° N	27.25° W	24	05/2012 - 12/2017	0.14
BHD	Baring Head Station	New Zealand	NOAA/INSTAAR	41.41° S	174.87° E	90	01/2012 - 11/2017	0.09
BRW	Barrow Atmospheric Baseline Observatory	United States	NOAA/INSTAAR	71.32° N	156.61° W	27	01/2012 - 12/2017	0.19
CBA	Cold Bay	United States	NOAA/INSTAAR	55.20° N	162.72° W	57	01/2012 - 12/2017	0.14
CGO	Cape Grim	Australia	NOAA/INSTAAR	40.68° S	144.69° E	164	01/2012 - 12/2017	0.12
KUM	Cape Kumukahi	United States	NOAA/INSTAAR	19.53° N	154.83° W	8	01/2012 - 12/2017	0.12
MEX	High Altitude Global Climate Observation Center	Mexico	NOAA/INSTAAR	18.98° N	97.31° W	4469	01/2012 - 12/2017	0.13
MHD	Mace Head	Ireland	NOAA/INSTAAR	53.33° N	9.90° W	26	01/2012 - 12/2017	0.17
MLO	Mauna Loa	United States	NOAA/INSTAAR	19.54° N	155.58° W	3437	01/2012 - 12/2017	0.12
NWR	Niwot Ridge	United States	NOAA/INSTAAR	40.05° N	105.59° W	3526	01/2012 - 12/2017	0.11
SMO	Tutuila	American Samoa	NOAA/INSTAAR	14.25° S	170.57° W	47	01/2012 - 12/2017	0.12
SPO	South Pole	United States	NOAA/INSTAAR	89.98° S	24.80° W	2821	01/2012 - 12/2017	0.11
SUM	Summit	Greenland	NOAA/INSTAAR	72.60° N	38.42° W	3214	01/2012 - 12/2017	0.13
WLG	Mt. Waliguan	Peoples Republic of China	NOAA/INSTAAR	36.28° N	100.91° E	3815	01/2012 - 12/2017	0.12
ZEP	Ny-Alesund	Norway and Sweden	NOAA/INSTAAR	78.91° N	11.89° E	479	01/2012 - 12/2017	0.14

Table S5. Global and regional methane emissions by source category and region ($\mathrm{TgCH_4\ yr^{-1}}$) for all configurations and averaged over the 2014-2015 period.

Others										
	PRIOR REF	NOISO	REF	S1	S2	S3	T1	T2	T3	T4
BB	1	1	1	1	1	1	1	1	1	1
AGW	4	4	4	4	4	4	4	4	4	4
FF	5	5	5	5	5	5	5	5	5	5
NAT	8	8	8	8	8	8	8	8	8	8
WET	2	2	2	2	2	2	2	2	2	2
Total	19	19	19	19	19	19	19	19	19	19
U.S										
	PRIOR REF	NOISO	REF	S1	S2	S3	T1	T2	T3	T4
BB	1	1	1	1	1	1	1	1	1	1
AGW	21	22	22	22	22	22	22	22	22	21
FF	13	13	14	14	14	14	14	14	14	15
NAT	2	2	2	2	2	2	2	2	2	2
WET	17	17	17	17	17	17	17	17	16	16
Total	55	55	56	56	56	56	56	56	56	56
Canada										
	PRIOR REF	NOISO	REF	S1	S2	S3	T1	T2	T3	T4
BB	2	1	2	2	2	2	2	2	3	3
AGW	2	2	2	2	2	2	2	2	2	2
FF	2	2	2	2	2	2	2	2	2	2
NAT	1	1	1	1	1	1	1	1	1	1
WET	27	23	21	21	21	21	22	23	16	18
Total	34	30	29	29	29	29	30	30	24	26
South America										
	PRIOR REF	NOISO	REF	S1	S2	S3	T1	T2	T3	T4
BB	2	2	2	2	2	2	2	2	2	3
AGW	29	31	30	30	30	31	30	30	29	30
FF	5	6	6	6	6	6	6	6	6	6
NAT	5	5	5	5	5	5	5	5	5	5
WET	49	55	53	53	53	54	53	52	51	50
Total	91	99	96	96	97	97	96	96	93	93
Africa										
	PRIOR REF	NOISO	REF	S1	S2	S3	T1	T2	T3	T4
BB	8	8	9	9	9	9	9	9	9	10
AGW	25	26	25	25	25	25	25	25	25	25
FF	13	13	14	14	14	14	14	14	14	15
NAT	4	4	4	4	4	4	4	4	4	4
WET	26	28	28	28	28	28	28	27	27	26
Total	77	80	80	80	80	80	80	80	80	80

Table S5. Global and regional methane emissions by source category and region ($\mathrm{TgCH_4\ yr^{-1}}$) for all configurations and averaged over the 2014-2015 period.

Europe										
	PRIOR REF	NOISO	REF	S1	S2	S3	T1	T2	T3	T4
BB	1	1	1	1	1	1	1	1	1	1
AGW	21	20	20	20	20	20	20	20	20	19
FF	6	6	6	6	6	6	6	6	7	7
NAT	2	2	2	2	2	2	2	2	2	2
WET	4	4	4	4	4	4	4	4	4	4
Total	34	33	34	34	34	34	34	33	34	33
Russia										
	PRIOR REF	NOISO	REF	S1	S2	S3	T1	T2	T3	T4
BB	2	2	2	2	2	2	2	2	2	2
AGW	5	5	5	5	5	5	5	5	5	5
FF	12	12	12	12	12	12	12	12	13	13
NAT	3	3	3	3	3	3	3	3	3	3
WET	13	12	12	12	13	13	13	13	11	12
Total	35	34	35	35	35	35	36	35	35	35
Temperate Asia										
	PRIOR REF	NOISO	REF	S1	S2	S3	T1	T2	T3	T4
BB	3	3	3	3	3	3	3	3	3	3
AGW	55	56	54	54	55	54	54	54	51	51
FF	26	27	28	28	28	28	29	29	30	31
NAT	7	7	7	7	7	7	7	7	7	7
WET	12	13	13	13	13	13	13	12	12	11
Total	103	105	105	106	106	105	105	105	104	104
China										
	PRIOR REF	NOISO	REF	S1	S2	S3	T1	T2	T3	T4
BB	5	5	5	5	5	5	5	5	5	5
AGW	36	32	29	28	29	29	31	29	26	26
FF	25	19	24	24	23	23	21	22	33	29
NAT	1	1	1	1	1	1	1	1	1	1
WET	5	5	5	5	5	5	5	5	5	5
Total	72	61	64	63	63	63	63	62	70	66
South East Asia										
	PRIOR REF	NOISO	REF	S1	S2	S3	T1	T2	T3	T4
BB	8	9	11	10	10	10	10	11	15	18
AGW	22	23	23	23	23	23	22	23	22	22
FF	7	7	8	8	8	8	8	8	8	8
NAT	3	4	4	4	4	4	3	4	4	4
WET	22	23	22	22	22	22	22	22	22	21
Total	63	66	66	66	67	66	66	67	70	72

Table S5. Global and regional methane emissions by emission category for all configurations and averaged over 2014-2015.

Oceania										
	PRIOR REF	NOISO	REF	S1	S2	S3	T1	T2	T3	T4
BB	0	0	1	1	1	1	1	1	1	1
AGW	5	5	4	4	4	4	4	4	4	4
FF	2	2	2	2	2	2	2	2	2	2
NAT	1	1	1	1	1	1	1	1	1	1
WET	3	3	3	3	3	3	3	3	3	3
Total	11	11	11	11	11	11	11	11	11	11
Global										
	PRIOR REF	NOISO	REF	S1	S2	S3	T1	T2	T3	T4
BB	33	33	37	37	37	36	37	38	44	47
AGW	226	226	220	219	221	220	220	220	211	210
FF	116	111	119	120	120	119	118	119	134	132
NAT	38	38	38	39	39	38	39	39	39	39
WET	180	185	180	179	181	181	182	180	169	167
Total	593	594	594	594	597	594	595	594	596	595

Table S6. Global and regional source signatures by emission category (‰) for all configurations and flux-weighted averaged with posterior fluxes 2014-2015.

Others									
	PRIOR REF	REF	S1	S2	S3	T1	T2	T3	T4
BB	-24.8	-24.4	-24.4	-24.4	-24.5	-24.4	-22.3	-24.8	-22.6
AGW	-57.2	-56.9	-56.8	-56.8	-56.9	-57.0	-58.7	-57.1	-59.1
FF	-45.1	-44.9	-44.9	-44.9	-44.9	-44.9	-43.2	-45.1	-43.4
NAT	-42.7	-42.7	-42.7	-42.7	-42.7	-42.6	-49.9	-42.7	-49.9
WET	-60.1	-59.9	-59.9	-59.9	-59.9	-59.9	-60.0	-60.1	-60.2
Total	-47.3	-47.1	-47.0	-47.0	-47.1	-47.0	-49.8	-47.0	-49.7
U.S									
	PRIOR REF	REF	S1	S2	S3	T1	T2	T3	T4
BB	-24.8	-24.7	-24.7	-24.7	-24.7	-24.7	-22.7	-24.8	-22.7
AGW	-59.0	-58.5	-58.4	-58.4	-58.4	-58.5	-58.5	-58.9	-59.1
FF	-45.3	-44.8	-44.7	-44.7	-44.7	-44.7	-43.0	-45.2	-43.4
NAT	-49.7	-49.6	-49.6	-49.6	-49.7	-49.6	-49.9	-49.6	-49.9
WET	-61.7	-60.6	-60.4	-60.5	-60.7	-60.3	-60.3	-61.3	-61.0
Total	-55.6	-54.8	-54.6	-54.7	-54.8	-54.7	-54.2	-55.0	-54.4
Canada									
	PRIOR REF	REF	S1	S2	S3	T1	T2	T3	T4
BB	-24.8	-24.0	-24.0	-24.0	-24.3	-24.0	-22.5	-24.8	-23.0
AGW	-57.2	-56.8	-56.7	-56.8	-56.8	-56.8	-58.6	-57.1	-59.1
FF	-54.7	-54.2	-54.1	-54.1	-54.1	-54.1	-43.0	-54.7	-43.4
NAT	-44.8	-44.8	-44.8	-44.8	-44.8	-44.8	-49.9	-44.8	-49.9
WET	-70.0	-66.8	-66.2	-66.5	-67.1	-65.8	-59.7	-69.4	-62.1
Total	-65.2	-61.3	-60.6	-61.0	-61.6	-60.4	-55.6	-60.6	-55.8
South America									
	PRIOR REF	REF	S1	S2	S3	T1	T2	T3	T4
BB	-22.0	-21.8	-21.8	-21.8	-21.9	-21.8	-22.5	-22.0	-22.6
AGW	-58.8	-58.3	-58.2	-58.3	-58.3	-58.3	-58.4	-58.8	-59.1
FF	-46.5	-46.3	-46.3	-46.3	-46.3	-46.3	-43.3	-46.5	-43.4
NAT	-57.2	-57.2	-57.2	-57.2	-57.2	-57.2	-49.9	-57.2	-49.9
WET	-57.8	-56.6	-56.4	-56.5	-56.6	-56.2	-58.2	-57.7	-59.7
Total	-56.6	-55.7	-55.6	-55.7	-55.8	-55.5	-56.1	-56.4	-57.0
Africa									
	PRIOR REF	REF	S1	S2	S3	T1	T2	T3	T4
BB	-21.0	-20.9	-20.9	-20.9	-20.9	-20.9	-22.4	-21.0	-22.6
AGW	-59.7	-59.4	-59.3	-59.3	-59.4	-59.4	-58.7	-59.7	-59.1
FF	-44.0	-43.7	-43.6	-43.6	-43.7	-43.6	-43.1	-43.9	-43.4
NAT	-55.7	-55.7	-55.6	-55.6	-55.7	-55.6	-49.9	-55.7	-49.9
WET	-55.4	-54.7	-54.6	-54.6	-54.7	-54.5	-59.0	-55.3	-59.9
Total	-51.2	-50.6	-50.6	-50.6	-50.7	-50.5	-51.5	-50.6	-51.6

Table S6. Global and regional source signatures by emission category (‰) for all configurations and flux-weighted averaged with posterior fluxes 2014-2015.

Europe									
	PRIOR REF	REF	S1	S2	S3	T1	T2	T3	T4
BB	-24.4	-24.3	-24.3	-24.3	-24.3	-24.3	-22.6	-24.4	-22.6
AGW	-58.7	-57.9	-57.8	-57.9	-58.0	-57.9	-58.3	-58.7	-59.1
FF	-44.4	-44.1	-44.1	-44.1	-44.1	-44.2	-43.1	-44.4	-43.4
NAT	-47.5	-47.4	-47.4	-47.4	-47.4	-47.4	-49.9	-47.5	-49.9
WET	-66.7	-66.4	-66.4	-66.4	-66.4	-66.3	-61.0	-66.6	-61.2
Total	-55.4	-54.7	-54.7	-54.7	-54.8	-54.8	-54.2	-55.1	-54.5
Russia									
	PRIOR REF	REF	S1	S2	S3	T1	T2	T3	T4
BB	-24.8	-24.5	-24.5	-24.5	-24.6	-24.5	-22.7	-24.8	-22.9
AGW	-56.0	-55.6	-55.6	-55.6	-55.7	-55.6	-58.7	-55.9	-59.1
FF	-44.3	-43.9	-43.8	-43.9	-44.0	-43.9	-43.0	-44.3	-43.4
NAT	-47.8	-47.8	-47.7	-47.7	-47.8	-47.7	-49.9	-47.8	-49.9
WET	-68.7	-67.2	-67.0	-67.2	-67.5	-66.9	-61.3	-68.4	-62.3
Total	-54.5	-53.2	-53.1	-53.3	-53.6	-53.2	-51.4	-53.0	-51.3
Temperate Asia									
	PRIOR REF	REF	S1	S2	S3	T1	T2	T3	T4
BB	-22.5	-22.4	-22.4	-22.4	-22.4	-22.4	-22.5	-22.4	-22.6
AGW	-59.2	-57.7	-57.5	-57.6	-57.6	-58.2	-57.3	-59.2	-59.1
FF	-44.0	-43.4	-43.4	-43.4	-43.4	-43.3	-42.7	-44.1	-43.4
NAT	-50.0	-49.7	-49.7	-49.7	-49.8	-49.7	-49.7	-50.0	-49.9
WET	-58.5	-57.4	-57.2	-57.3	-57.5	-57.1	-60.2	-58.5	-61.4
Total	-53.6	-52.3	-52.1	-52.2	-52.3	-52.4	-52.1	-52.9	-52.8
China									
	PRIOR REF	REF	S1	S2	S3	T1	T2	T3	T4
BB	-22.3	-22.2	-22.1	-22.2	-22.2	-22.1	-22.4	-22.3	-22.6
AGW	-58.8	-57.2	-57.0	-57.1	-57.3	-58.1	-57.0	-58.9	-59.1
FF	-37.7	-36.5	-36.4	-36.4	-36.7	-36.6	-41.5	-37.4	-43.4
NAT	-49.0	-49.0	-49.0	-49.0	-49.0	-49.0	-49.9	-49.0	-49.9
WET	-58.5	-58.1	-58.0	-58.1	-58.1	-58.0	-60.6	-58.5	-61.2
Total	-48.9	-46.8	-46.5	-46.7	-47.0	-48.0	-48.9	-45.8	-49.2
South East Asia									
	PRIOR REF	REF	S1	S2	S3	T1	T2	T3	T4
BB	-23.1	-21.7	-21.9	-21.6	-22.2	-21.7	-21.2	-22.9	-22.7
AGW	-59.8	-58.8	-58.7	-58.8	-58.8	-59.4	-57.9	-59.8	-59.1
FF	-46.0	-45.7	-45.7	-45.7	-45.7	-45.7	-43.1	-46.0	-43.4
NAT	-54.2	-54.1	-54.1	-54.1	-54.1	-54.1	-49.9	-54.1	-49.9
WET	-58.5	-57.9	-57.9	-57.9	-58.0	-57.8	-59.3	-58.5	-60.0
Total	-52.6	-50.9	-50.9	-50.9	-51.2	-51.1	-50.1	-49.7	-48.5

Table S6. Global and regional source signatures by emission category (‰) for all configurations and flux-weighted averaged with posterior fluxes 2014-2015.

Oceania									
	PRIOR REF	REF	S1	S2	S3	T1	T2	T3	T4
BB	-24.8	-24.7	-24.7	-24.7	-24.7	-24.7	-22.6	-24.8	-22.6
AGW	-62.8	-62.7	-62.7	-62.7	-62.7	-62.6	-58.9	-62.9	-59.1
FF	-50.7	-50.6	-50.6	-50.6	-50.6	-50.6	-43.3	-50.7	-43.4
NAT	-49.1	-49.1	-49.1	-49.1	-49.1	-49.1	-49.9	-49.1	-49.9
WET	-56.5	-56.4	-56.3	-56.4	-56.4	-56.3	-59.2	-56.5	-59.4
Total	-56.0	-55.8	-55.7	-55.7	-55.8	-55.7	-53.9	-55.8	-54.0
Global									
	PRIOR REF	REF	S1	S2	S3	T1	T2	T3	T4
BB	-22.6	-22.1	-22.2	-22.1	-22.3	-22.1	-22.0	-22.7	-22.7
AGW	-59.1	-58.2	-58.0	-58.1	-58.2	-58.4	-58.0	-59.1	-59.1
FF	-43.4	-42.9	-42.9	-42.9	-43.1	-43.1	-42.7	-43.1	-43.4
NAT	-50.0	-49.9	-49.9	-49.9	-49.9	-49.8	-49.9	-49.9	-49.9
WET	-60.8	-59.1	-58.9	-59.0	-59.2	-58.8	-59.4	-59.9	-60.6
Total	-53.9	-52.6	-52.5	-52.6	-52.8	-52.7	-52.5	-52.4	-52.6

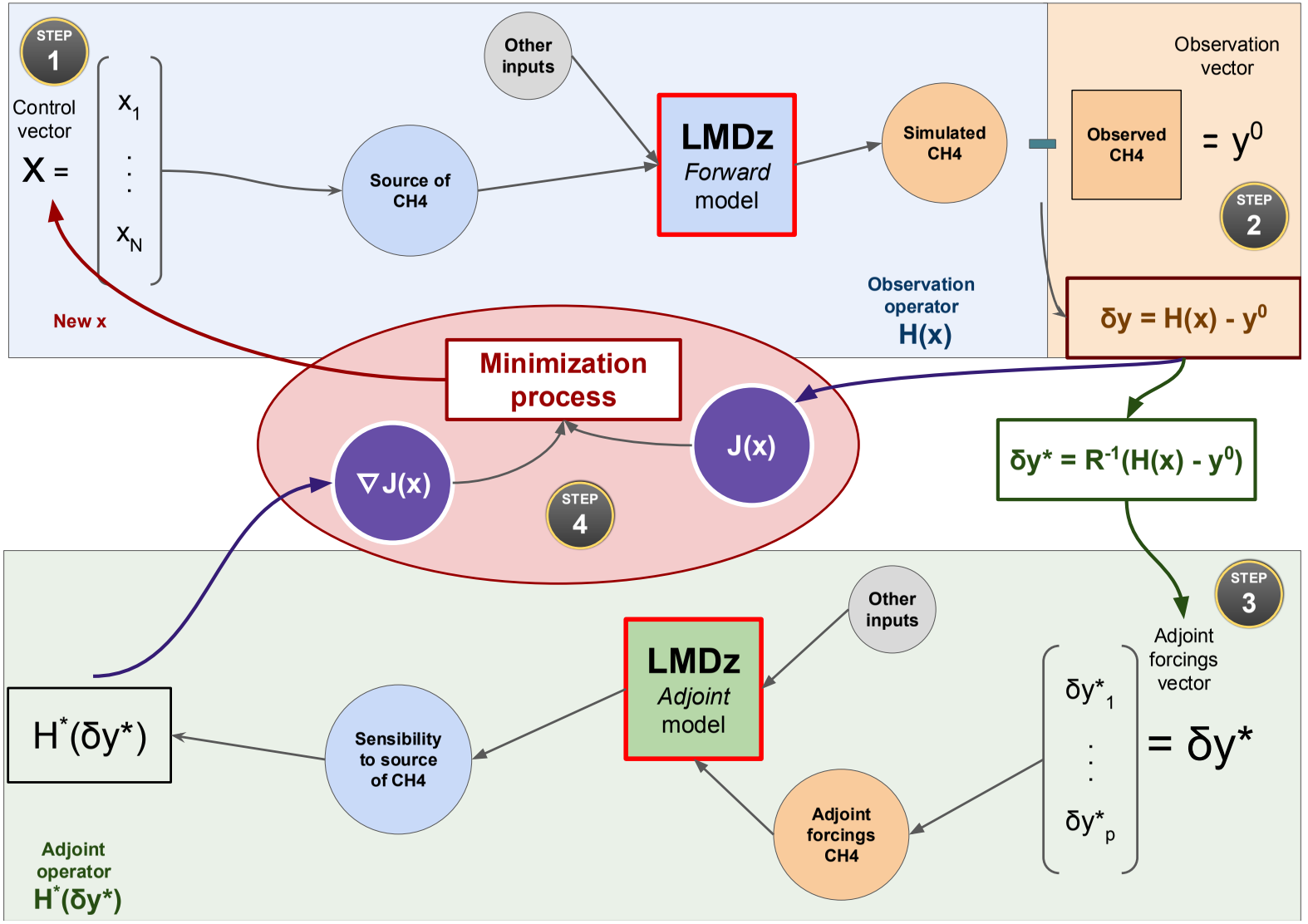

Figure S1. The minimization iteration process used in the previous system. The "step" black circles with gold border indicates the reading direction to follow. Step 1 (blue rectangle) refers to a forward run. Step 2 (orange rectangle) refers to the forward and adjoint operations required to compare observations and simulated values. Step 3 (green rectangle) refers to an adjoint run. This step must be read from the right to the left. Step 4 (red ellipse) refers to the minimization of the cost function operated by the dedicated minimization algorithm. Note that results of step 2 are used both in the minimization process (red ellipse) and as inputs for step 3.

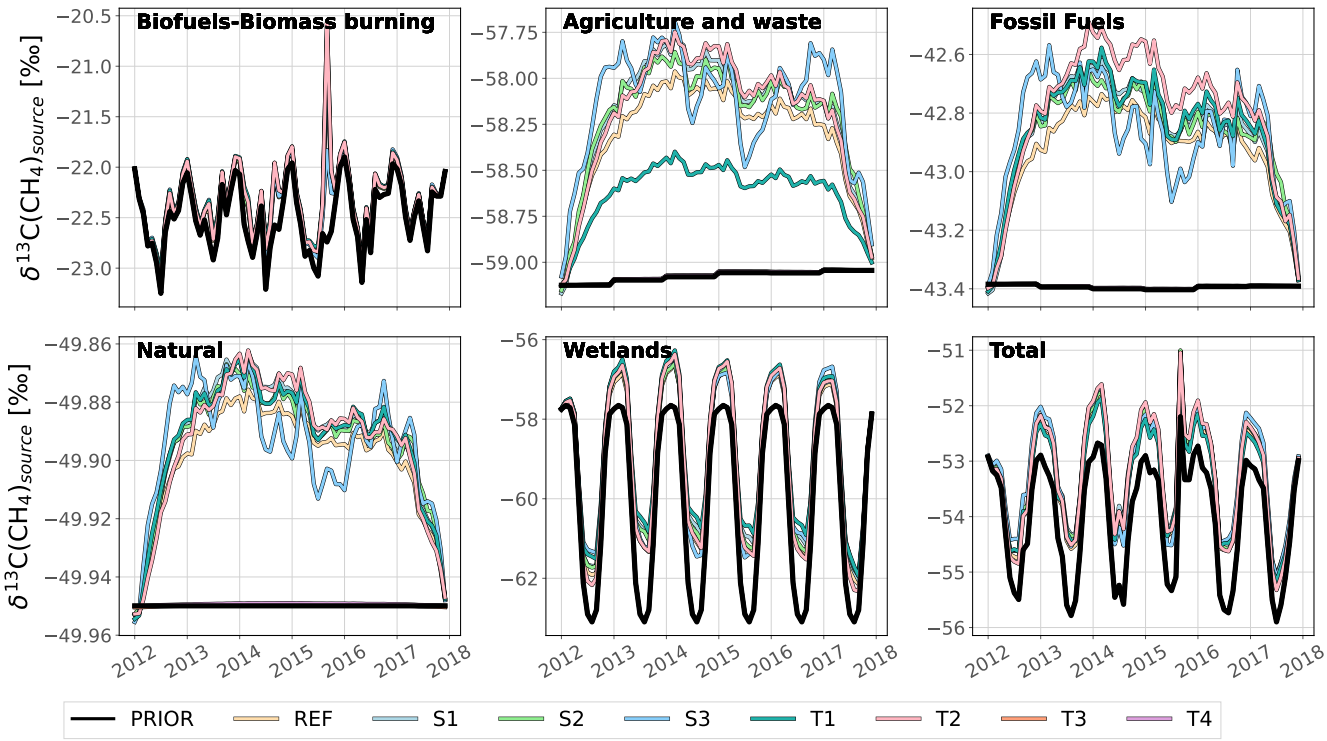

Figure S2. Prior (black line) and posterior (others) source signatures for each category and each configuration. The source signatures are computed using a flux-weighted average with prior fluxes.

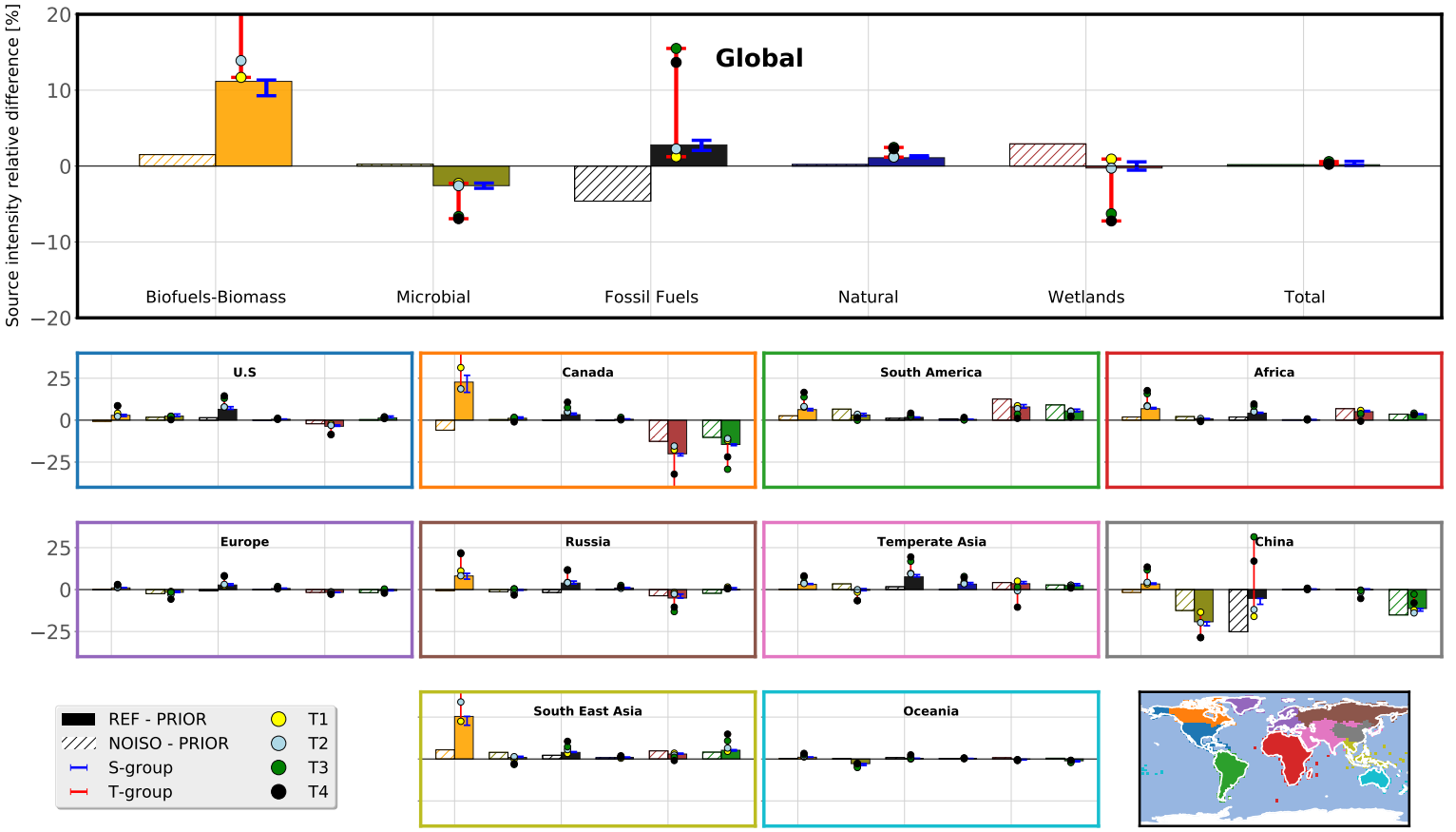

Figure S3. Same as Figure 6 from the main paper but with relative values (in %). Several error ranges are not fully displayed to improve clarity.

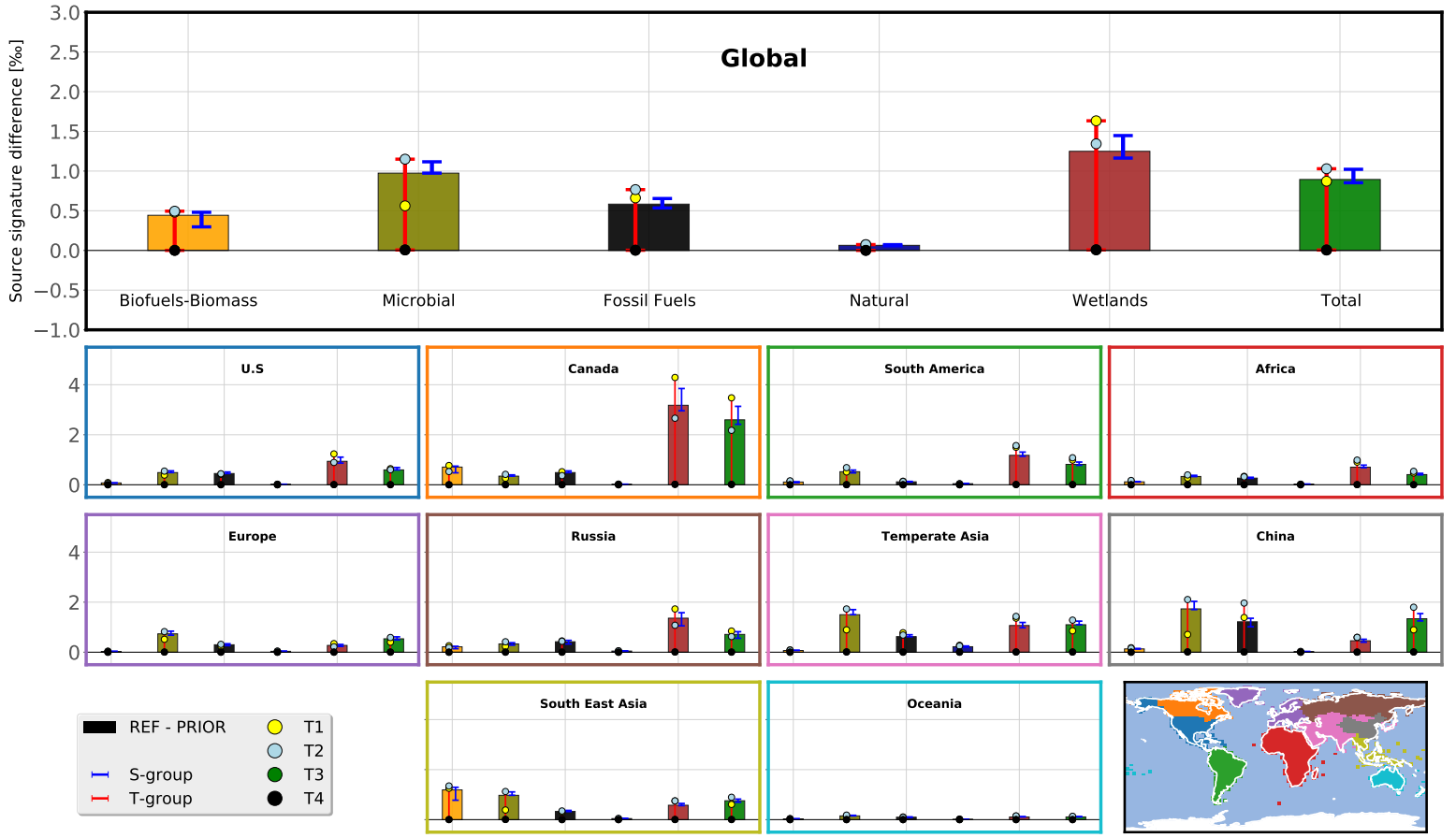

Figure S4. Same as Figure 7 from the main paper but prior fluxes are used to compute flux-weighted averages.

References

Berchet, A., Sollum, E., Thompson, R. L., Pison, I., Thanwerdas, J., Broquet, G., Chevallier, F., Aalto, T., Berchet, A., Bergamaschi, P., Brunner, D., Engelen, R., Fortems-Cheiney, A., Gerbig, C., Groot Zwaaftink, C. D., Haussaire, J.-M., Henne, S., Houweling, S., Karstens, U., Kutsch, W. L., Luijkx, I. T., Monteil, G., Palmer, P. I., van Peet, J. C. A., Peters, W., Peylin, P., Potier, E., Rödenbeck, C., Saunois, M., Scholze, M., Tsuruta, A., and Zhao, Y.: The Community Inversion Framework v1.0: a unified system for atmospheric inversion studies, Geoscientific Model Development, 14, 5331–5354, https://doi.org/10.5194/gmd-14-5331-2021, 2021.

Bergamaschi, P., Lubina, C., Königstedt, R., Fischer, H., Veltkamp, A. C., and Zwaagstra, O.: Stable isotopic signatures (δ^{13}C, δD) of methane from European landfill sites, Journal of Geophysical Research: Atmospheres, 103, 8251–8265, https://doi.org/10.1029/98JD00105, 1998.

Bousquet, P., Ciais, P., Miller, J. B., Dlugokencky, E. J., Hauglustaine, D. A., Prigent, C., Van der Werf, G. R., Peylin, P., Brunke, E.-G., Carouge, C., Langenfelds, R. L., Lathière, J., Papa, F., Ramonet, M., Schmidt, M., Steele, L. P., Tyler, S. C., and White, J.: Contribution of anthropogenic and natural sources to atmospheric methane variability, Nature, 443, 439–443, https://doi.org/10.1038/nature05132, 2006.

Brunskill, G. J., Burns, K. A., and Zagorskis, I.: Natural flux of greenhouse methane from the Timor Sea to the atmosphere, Journal of Geophysical Research: Biogeosciences, 116, https://doi.org/10.1029/2010JG001444, 2011.

Bréas, O., Guillou, C., Reniero, F., and Wada, E.: The Global Methane Cycle: Isotopes and Mixing Ratios, Sources and Sinks, Isotopes in Environmental and Health Studies, 37, 257–379, https://doi.org/10.1080/10256010108033302, 2001.

Burkholder, J. B., Abbatt, J. P. D., Huie, R. E., Kurylo, M. J., Wilmouth, D. M., Sander, S. P., Barker, J. R., Kolb, C. E., Orkin, V. L., and Wine, P. H.: JPL Publication 15-10: Chemical Kinetics and Photochemical Data for Use in Atmospheric Studies, p. 1392, 2015.

Cantrell, C. A., Shetter, R. E., McDaniel, A. H., Calvert, J. G., Davidson, J. A., Lowe, D. C., Tyler, S. C., Cicerone, R. J., and Greenberg, J. P.: Carbon kinetic isotope effect in the oxidation of methane by the hydroxyl radical, Journal of Geophysical Research: Atmospheres, 95, 22 455–22 462, https://doi.org/https://doi.org/10.1029/JD095iD13p22455, 1990.

Chanton, J. P., Rutkowski, C. M., and Mosher, B.: Quantifying Methane Oxidation from Landfills Using Stable Isotope Analysis of Downwind Plumes, Environmental Science & Technology, 33, 3755–3760, https://doi.org/10.1021/es9904033, 1999.

Chanton, J. P., Rutkowski, C. M., Schwartz, C. C., Ward, D. E., and Boring, L.: Factors influencing the stable carbon isotopic signature of methane from combustion and biomass burning, Journal of Geophysical Research: Atmospheres, 105, 1867–1877, https://doi.org/10.1029/1999JD900909, 2000.

Folberth, G. A., Hauglustaine, D. A., Lathière, J., and Brocheton, F.: Interactive chemistry in the Laboratoire de Météorologie Dynamique general circulation model: model description and impact analysis of biogenic hydrocarbons on tropospheric chemistry, Atmospheric Chemistry and Physics, 6, 2273–2319, https://doi.org/10.5194/acp-6-2273-2006, 2006.

Hauglustaine, D. A., Hourdin, F., Jourdain, L., Filiberti, M.-A., Walters, S., Lamarque, J.-F., and Holland, E. A.: Interactive chemistry in the Laboratoire de Météorologie Dynamique general circulation model: Description and background tropospheric chemistry evaluation, Journal of Geophysical Research: Atmospheres, 109, https://doi.org/10.1029/2003JD003957, 2004.

Holmes, M. E., Sansone, F. J., Rust, T. M., and Popp, B. N.: Methane production, consumption, and air-sea exchange in the open ocean: An Evaluation based on carbon isotopic ratios, Global Biogeochemical Cycles, 14, 1–10, https://doi.org/10.1029/1999GB001209, 2000.

King, S. L., Quay, P. D., and Lansdown, J. M.: The ^{13}C/^{12}C kinetic isotope effect for soil oxidation of methane at ambient atmospheric concentrations, Journal of Geophysical Research: Atmospheres, 94, 18 273–18 277, https://doi.org/10.1029/JD094iD15p18273, 1989.

Levin, I., Bergamaschi, P., Dörr, H., and Trapp, D.: Stable isotopic signature of methane from major sources in Germany, Chemosphere, 26, 161–177, https://doi.org/10.1016/0045-6535(93)90419-6, 1993.

Reeburgh, W. S., Hirsch, A. I., Sansone, F. J., Popp, B. N., and Rust, T. M.: Carbon kinetic isotope effect accompanying microbial oxidation of methane in boreal forest soils, Geochimica et Cosmochimica Acta, 61, 4761–4767, https://doi.org/10.1016/S0016-7037(97)00277-9, 1997.

Rice, A. L., Butenhoff, C. L., Teama, D. G., Röger, F. H., Khalil, M. A. K., and Rasmussen, R. A.: Atmospheric methane isotopic record favors fossil sources flat in 1980s and 1990s with recent increase, Proceedings of the National Academy of Sciences, 113, 10 791–10 796, https://doi.org/10.1073/pnas.1522923113, 2016.

Ridgwell, A. J., Marshall, S. J., and Gregson, K.: Consumption of atmospheric methane by soils: A process-based model, Global Biogeochemical Cycles, 13, 59–70, https://doi.org/10.1029/1998GB900004, 1999.

Sansone, F. J., Popp, B. N., Gasc, A., Graham, A. W., and Rust, T. M.: Highly elevated methane in the eastern tropical North Pacific and associated isotopically enriched fluxes to the atmosphere, Geophysical Research Letters, 28, 4567–4570, https://doi.org/10.1029/2001GL013460, 2001.

Saueressig, G., Bergamaschi, P., Crowley, J. N., Fischer, H., and Harris, G. W.: Carbon kinetic isotope effect in the reaction of CH_4 with Cl atoms, Geophysical Research Letters, 22, 1225–1228, https://doi.org/10.1029/95GL00881, 1995.

Saueressig, G., Crowley, J. N., Bergamaschi, P., Brühl, C., Brenninkmeijer, C. A. M., and Fischer, H.: Carbon 13 and D kinetic isotope effects in the reactions of CH_4 with O(1 D) and OH: New laboratory measurements and their implications for the isotopic composition of stratospheric methane, Journal of Geophysical Research: Atmospheres, 106, 23 127–23 138, https://doi.org/10.1029/2000JD000120, 2001.

Snover, A. K. and Quay, P. D.: Hydrogen and carbon kinetic isotope effects during soil uptake of atmospheric methane, Global Biogeochemical Cycles, 14, 25–39, https://doi.org/10.1029/1999GB900089, 2000.

Townsend-Small, A., Tyler, S. C., Pataki, D. E., Xu, X., and Christensen, L. E.: Isotopic measurements of atmospheric methane in Los Angeles, California, USA: Influence of "fugitive" fossil fuel emissions, Journal of Geophysical Research: Atmospheres, 117, https://doi.org/10.1029/2011JD016826, 2012.

Tyler, S. C., Crill, P. M., and Brailsford, G. W.: $^{13}C^{12}C$ Fractionation of methane during oxidation in a temperate forested soil, Geochimica et Cosmochimica Acta, 58, 1625–1633, https://doi.org/10.1016/0016-7037(94)90564-9, 1994.

Wang, X., Jacob, D. J., Eastham, S. D., Sulprizio, M. P., Zhu, L., Chen, Q., Alexander, B., Sherwen, T., Evans, M. J., Lee, B. H., Haskins, J. D., Lopez-Hilfiker, F. D., Thornton, J. A., Huey, G. L., and Liao, H.: The role of chlorine in global tropospheric chemistry, Atmospheric Chemistry and Physics, 19, 3981–4003, https://doi.org/10.5194/acp-19-3981-2019, 2019.

Yamada, K., Ozaki, Y., Nakagawa, F., Sudo, S., Tsuruta, H., and Yoshida, N.: Hydrogen and carbon isotopic measurements of methane from agricultural combustion: Implications for isotopic signatures of global biomass burning sources, Journal of Geophysical Research, 111, D16 306, https://doi.org/10.1029/2005JD006750, 2006.